Robustness of electronic screening effects in electron spectroscopies: Example of V_2O_5

Vitaly Gorelov, Lucia Reining, Walter R. L. Lambrecht, Matteo Gatti

Robustness of electronic screening effects in electron spectroscopies: example of V_2O_5

Vitaly Gorelov,[1,2] Lucia Reining,[1,2] Walter R. L. Lambrecht,[3] and Matteo Gatti[1,2,4]

[1] *LSI, CNRS, CEA/DRF/IRAMIS, École Polytechnique, Institut Polytechnique de Paris, F-91120 Palaiseau, France*

[2] *European Theoretical Spectroscopy Facility*

[3] *Department of Physics, Case Western Reserve University, Cleveland, OH-441-6-7079, USA*

[4] *Synchrotron SOLEIL, L'Orme des Merisiers Saint-Aubin, BP 48 F-91192 Gif-sur-Yvette, France*

(Dated: February 6, 2023)

In bulk and low-dimensional extended systems, the screening of excitations by the electron cloud is a key feature governing spectroscopic properties. Widely used computational approaches, especially in the framework of many-body perturbation theory, such as the GW approximation and the resulting approximate Bethe-Salpeter equation, are explicitly formulated in terms of the screened Coulomb interaction. In the present work we explore the effect of screening in absorption and electron energy loss spectroscopy, concentrating on the effect of local distortions on the screening and elucidating the resulting changes in the various spectra. Using the layered bulk oxide V_2O_5 as prototype material, we show in which way local distortions affect the screening, and in which way changes in the screening impact electron energy loss and absorption spectra including excitons. We highlight cancellations that make many-body effects in the spectra very robust with respect to structural modifications, while the band structure undergoes significant changes and the nature of the excitations may also be affected. This yields insight concerning the structure-properties relations that are crucial for the use of V_2O_5 as energy storage material, and more generally, that may be used to optimize the analysis and the calculation of electronic spectra in complex materials.

I. INTRODUCTION

Electronic excitations determine materials properties and functionalities that are crucial for a wide range of technological applications. Their theoretical analysis and prediction can therefore accelerate the discovery and design of materials with tailored properties. However, this remains a challenging problem for two main reasons: the effect of the electronic interactions and the inherent complexity of real materials. On the one hand, the electron-electron interaction strongly affects the excitation spectra of materials with respect to an independent-particle picture[1]. The Coulomb interaction is, in particular, at the origin of the collective excitations of the electronic charge, known as plasmons[2], and it is responsible for the formation of bound electron-hole pairs, termed excitons[3]. Plasmons and excitons characterise the dielectric and optical properties of materials and play a key role as energy carriers for all energy conversion and storage technologies. They are the central objects of plasmonics and excitonics, respectively, where their study is of fundamental importance in order to improve the efficiency of optoelectronic devices while reducing their size[4,5]. On the other hand, real materials differ in several ways from the ideal picture of perfectly periodic crystals that is usually assumed in the theoretical simulation of electronic excitation spectra. Besides the thermal motion of the atoms around their equilibrium positions, or the presence of defects such as vacancies and impurities, static atomic displacements and tiltings can make the atomic local environment different from the macroscopically averaged crystal structure that is determined from X-ray diffraction (XRD) data. Especially in transition metal compounds, where the electrons remain tightly localised around the ions, the electronic properties can be strongly affected by different local environments due to positional or magnetic symmetry breakings[6–9].

In this context, vanadium pentoxide V_2O_5 is a particularly interesting case. It is an attractive material for a wide range of environmental applications, such as decontamination treatment, gas sensing, supply of clean and renewable energy (including photocatalysis and photovoltaics), energy storage (for rechargeable lithium-ion batteries), and smart windows (thanks to its electrochromic properties)[10–20].

V_2O_5 has a peculiar layered crystal structure[21]. The layers, stacked along the z direction, are made of ladder structures with V-O zigzag chains forming the legs along the y direction which are connected by V-O-V rungs along x (see Fig. 1). Besides the chain O_c atoms in the legs and bridge O_b atoms in the rungs, a third kind of oxygen atoms, called vanadyl oxygen O_v, are located just above or below the V atoms. The resulting basic units are VO_5 pyramids formed by a vanadium atom and its five nearest oxygen neighbors (see Fig. 1). In each layer, pairs of VO_5 pyramids point along the $+z$ direction, alternating with pairs of pyramids pointing in the opposite $-z$ direction. VO_6 octahedra, which are more common in other vanadates, can be formed, although strongly distorted, only by adding to the group also another O_v atom from a neighboring pyramid.

The peculiar crystal structure of V_2O_5 is directly reflected into its electronic properties. Its low-dimensional nature is revealed by the weakly dispersing top-valence and bottom-conduction bands, which are separated by a relatively large indirect gap [see Fig. 1(c)]. Consistently with the ionic picture of a d^0 configuration, the valence band is mainly occupied by O $2p$ electrons, while the

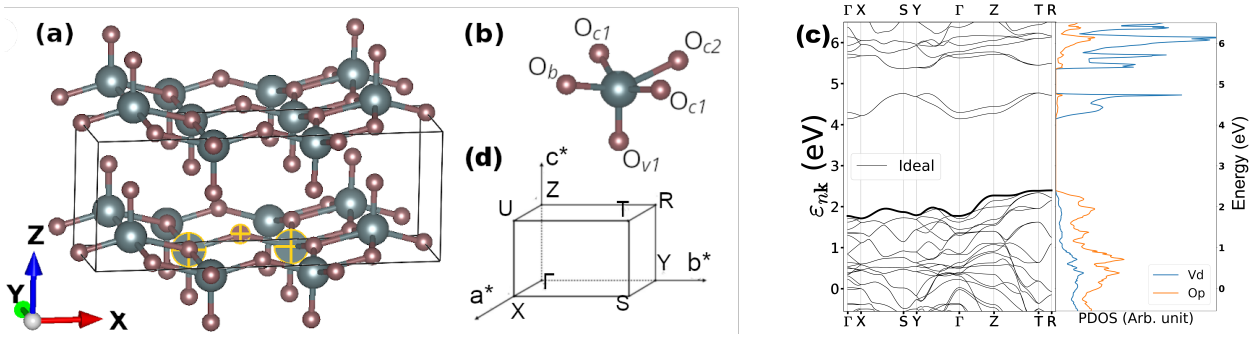

FIG. 1: Crystal structure and electronic properties of V_2O_5. (a) V_2O_5 layers are stacked along the z axis. V atoms are grey and O atoms are red. Highlighted in yellow is one V-O_b-V rung. The orthorhombic unit cell (space group $Pmmn$) is represented by the black lines. (b) The elementary units of the V_2O_5 layers are VO_5 pyramids, formed by one V atom, two chain oxygen atoms (O_{c1} and O_{c2}), one bridge oxygen (O_b) and one vanadyl oxygen (O_{v1}). The corresponding bond lengths are reported in Tab. I. (c) LDA band structure and corresponding projected density of states (PDOS). The bold line indicates the top valence band (see also Tab. III). (d) The first Brillouin zone with the labels of high symmetry **k** points.

conduction band is mainly due to V $3d$ states [as shown by the projected density of states (PDOS) in Fig. 1(c)]. However, O $2p$ and V $3d$ orbitals are also strongly hybridized. The V-O atomic distances determine the size of the bonding-antibonding splitting, which is larger for the short V-O_b and V-O_v bonds, and smaller for the longer V-O_c bonds (see Tab. I). The antibonding interactions also depend on the V $3d$ orbital symmetry. As analyzed in Refs.[22,23], the V d_{xy} orbitals have the weakest interaction with the nearest oxygen. In particular, the d_{xy} orbitals on the two vanadium atoms across a V-O_b-V rung that have equal parity are odd with respect to the m_x mirror plane passing through the bridge O_b. Hence, this d_{xy} pair has no interaction with the O_b p_y orbital and is orthogonal to both O_b p_x and O_b p_z orbitals. This structural peculiarity gives rise to a split-off band separated from the remaining conduction bands.

A strong interplay between atomic displacements and electronic properties is therefore expected in V_2O_5[24]. Indeed, Eyert and Höck[25] have shown that a hypothetical V_2O_5 crystal structure built from regular VO_6 octahedra, instead of the strongly distorted ones of the real structure, yields a metallic band structure. This strong sensitivity has also important practical consequences for lithium-ion batteries. While the processes of Li intercalation and delithiation do not modify V_2O_5 lattice parameters substantially, they perturb the local structure of the neighboring V_2O_5 pyramids, causing considerable band structure changes and a degradation of the electrochemical performance[26–31]. Moreover, charge carriers in V_2O_5 are interpreted as small polarons[32–36], i.e. the combination of electrons and accompanying lattice distortions, which hinders electronic and ionic mobilities. Addressing these issues is critical to enhance the performance of V_2O_5 as a clean energy functional material.

The following question, therefore, assumes special importance for the physics of V_2O_5: If the atoms of V_2O_5 are slightly displaced away from the equilibrium positions of the crystal structure determined from XRD data, what is the effect on the electronic properties and the excitation spectra? And are all properties affected in the same manner? If not, are there pieces of information that one could transfer from the ideal material to more complex structures, and can we understand why? In the present work, we contrast two different kinds of spectroscopy: optical absorption and electron energy loss spectroscopy (EELS), which are popular experimental techniques to determine, respectively, the excitonic and plasmonic properties of materials. Addressing this question at the specific example of V_2O_5 holds a more general relevance, concerning the impact of structural distortions on dielectric screening and many-body effects due to the electron-electron and electron-hole interactions.

The present paper is organised as follows. Sec. II summarizes the methodology and the computational parameters that have been employed for this study. The excitation spectra of V_2O_5 in its ideal crystal structure are first analysed in Sec. III A. The impact of prototypical atomic displacements on the absorption spectrum, the dark excitons, and the loss function is then investigated in Sec. III B. Finally, Sec. IV discusses the role of screening in various places and the importance of canceling of different contributions, while conclusions are drawn in Sec. V.

II. METHODOLOGY

A. Theoretical background

Electronic excitations spectra[37] of V_2O_5 have been calculated using linear-response time-dependent density functional theory[38,39] (TDDFT) and the Bethe-Salpeter equation[40] (BSE) in the framework of many-body perturbation theory[1] (MBPT).

Within TDDFT, the density-density response function

χ is obtained as a solution of the Dyson-like equation:

$$\chi = \chi_0 + \chi_0(v_c + f_{\rm xc})\chi, \quad (1)$$

where χ_0 is the independent-particle response function built with Kohn-Sham (KS) orbitals and energies, v_c is the Coulomb interaction, and $f_{\rm xc}$ is exchange-correlation (xc) kernel that is the functional derivative of the KS xc potential $V_{\rm xc}$ with respect to the density. The simplest approximation is the random-phase approximation (RPA) that sets $f_{\rm xc} = 0$.

In reciprocal space, the response functions and the xc kernel are matrices in the reciprocal lattice vectors $\mathbf{G}$ and $\mathbf{G}'$, and functions of the frequency ω and the first-Brillouin-zone wavevector $\mathbf{q}$. The Coulomb interaction is $v_c(\mathbf{q}+\mathbf{G}) = 4\pi|\mathbf{q}+\mathbf{G}|^{-2}$. From the response function χ one can directly evaluate the inverse microscopic dielectric function:

$$\epsilon^{-1}_{\mathbf{G},\mathbf{G}'}(\mathbf{q},\omega) = \delta_{\mathbf{G},\mathbf{G}'} + v_c(\mathbf{q}+\mathbf{G})\chi_{\mathbf{G},\mathbf{G}'}(\mathbf{q},\omega), \quad (2)$$

and the macroscopic dielectric function from the averaging procedure[41,42]:

$$\epsilon_M(\mathbf{q},\omega) = \frac{1}{\epsilon^{-1}_{\mathbf{G}=\mathbf{G}'=0}(\mathbf{q},\omega)}. \quad (3)$$

Eq. (3) takes into account crystal local field effects (LFEs), because the dielectric matrix is inverted before the macroscopic average $\mathbf{G} = \mathbf{G}' = 0$ is taken. Neglecting LFEs would simply lead to: $\epsilon_M(\mathbf{q},\omega) \simeq \epsilon_{\mathbf{G}=\mathbf{G}'=0}(\mathbf{q},\omega)$. The optical absorption spectrum is given by the long-wavelength limit: $\epsilon_2(\omega) = \lim_{\mathbf{q}\to 0} \mathrm{Im}\,\epsilon_M(\mathbf{q},\omega)$, whereas the loss function measured by EELS as a function of the momentum transfer $\mathbf{q}$ is given by $-\mathrm{Im}\,\epsilon^{-1}_M(\mathbf{q},\omega)$. By expressing the loss function in terms of the real and imaginary parts of the dielectric function $\epsilon_M(\mathbf{q},\omega) = \epsilon_1(\mathbf{q},\omega) + i\epsilon_2(\mathbf{q},\omega)$, one has:

$$-\mathrm{Im}\,\epsilon^{-1}_M(\mathbf{q},\omega) = \frac{\epsilon_2(\mathbf{q},\omega)}{[\epsilon_1(\mathbf{q},\omega)]^2 + [\epsilon_2(\mathbf{q},\omega)]^2}.$$

Peaks of the loss function which match zeros of the real part of the dielectric function $\epsilon_1(\mathbf{q},\omega)$ correspond to plasmon resonances.

Within MBPT, the quasiparticle (QP) addition and removal energies that form the band structures of materials can be obtained from the poles of the one-particle Green's function $G(\mathbf{r},\mathbf{r}',\omega)$. The effects of the electron-electron interaction beyond the electrostatic Hartree potential are encoded in the self-energy $\Sigma_{\rm xc}(\mathbf{r},\mathbf{r}',\omega)$. In the GW approximation[43] (GWA), $\Sigma_{\rm xc}(\omega)$ is given by the convolution between $G(\omega)$ and the screened Coulomb interaction $W(\omega) = \epsilon^{-1}(\omega)v_c$ evaluated in the RPA. In the G_0W_0 scheme[44,45], the KS Green's function is used to build the RPA W_0 and the self-energy. Moreover, usually the QP energies $E_{n\mathbf{k}}$ are obtained as first-order perturbative corrections to the KS eigenvalues $\varepsilon_{n\mathbf{k}}$ as:

$$E_{n\mathbf{k}} = \varepsilon_{n\mathbf{k}} + Z_{n\mathbf{k}}\langle\varphi_{n\mathbf{k}}|\Sigma_{\rm xc}(\varepsilon_{n\mathbf{k}}) - V_{\rm xc}|\varphi_{n\mathbf{k}}\rangle, \quad (4)$$

where $\varphi_{n\mathbf{k}}$ are KS orbitals and the QP renormalization factors are $Z_{n\mathbf{k}} = \left[1 - \langle \frac{\partial\Sigma_{\rm xc}(\omega)}{\partial\omega}\Big|_{\varepsilon_{n\mathbf{k}}} \rangle\right]^{-1}$. Alternatively, QP energies and orbitals entering the GW self-energy are calculated self-consistently, notably within the quasiparticle self-consistent GW (QSGW) scheme[46]. While the QSGW results do not depend on the KS starting point, the calculations are computationally much more expensive than the G_0W_0 ones.

In principle, one can obtain also response properties exactly in MBPT, by solving the Bethe-Salpeter equation. Approximations are available that yield exciton properties of materials accurately[47–49]. In particular, in the GWA with a statically screened Coulomb interaction W, the BSE can be reformulated as an electron-hole (excitonic) Hamiltonian problem: $H_{\rm exc}A_\lambda = E_\lambda A_\lambda$. In the basis $|vc\mathbf{k}\rangle$ of resonant transitions between occupied $v\mathbf{k}$ and unoccupied states $c\mathbf{k}$, and neglecting the coupling with antiresonant transitions (Tamm-Dancoff approximation), the excitonic Hamiltonian reads:

$$\langle vc\mathbf{k}|H_{\rm exc}|v'c'\mathbf{k}'\rangle = E_{vc\mathbf{k}}\delta_{vv'}\delta_{cc'}\delta_{\mathbf{k}\mathbf{k}'} + \langle vc\mathbf{k}|\bar{v}_c - W|v'c'\mathbf{k}'\rangle. \quad (5)$$

Here $E_{vc\mathbf{k}} = E_{c\mathbf{k}} - E_{v\mathbf{k}}$ are the GWA transition energies between occupied and empty states, while the electron-hole interaction matrix elements are the sum of the attractive direct electron-hole interaction $-W$ and the repulsive electron-hole exchange interaction $\bar{v}_c$ given by the microscopic components (i.e., $\mathbf{G} \neq 0$) of the bare Coulomb interaction. In the Tamm-Dancoff approximation, which is usually a good approximation for semiconductors and insulators[37], the optical absorption spectrum is obtained from the eigenvectors $A^{vc\mathbf{k}}_\lambda$ and eigenvalues E_λ of the excitonic hamiltonian as:

$$\epsilon_2(\omega) = \lim_{\mathbf{q}\to 0}\frac{8\pi^2}{\Omega q^2}\sum_\lambda \left|\sum_{vc\mathbf{k}} A^{vc\mathbf{k}}_\lambda \tilde{\rho}_{vc\mathbf{k}}(\mathbf{q})\right|^2 \delta(\omega - E_\lambda), \quad (6)$$

where Ω is the crystal volume, and the oscillator strengths are $\tilde{\rho}_{vc\mathbf{k}}(\mathbf{q}) = \int \varphi^*_{v\mathbf{k}-\mathbf{q}}(\mathbf{r})e^{-i\mathbf{q}\cdot\mathbf{r}}\varphi_{c\mathbf{k}}(\mathbf{r})d\mathbf{r}$. With respect to the independent-particle approximation where the electron-hole interactions are neglected, peaks in the BSE absorption spectra are located at the exciton energies E_λ, instead of $E_{vc\mathbf{k}}$, and have modified intensities resulting from the mixing of the oscillator strengths that are modulated by the excitonic coefficients $A^{vc\mathbf{k}}_\lambda$. In this context, the exciton binding energy is defined as the energy difference between the minimum direct gap energy $E_{vc\mathbf{k}}$ and the exciton energy E_λ. Supposing that in the $\mathbf{q}\to 0$ limit the oscillator strengths $\sum_{vc\mathbf{k}} A^{vc\mathbf{k}}_\lambda \tilde{\rho}_{vc\mathbf{k}}$ are approximately proportional to $1/E_\lambda$, Eq. 6 reduces to $\epsilon_2(\omega) \propto \mathrm{JDOS}(\omega)$, with the joint density of states $\mathrm{JDOS}(\omega) = \frac{2}{\Omega\omega^2}\sum_\lambda \delta(\omega - E_\lambda)$.

B. Computational details

In our calculations, the ideal crystal structure of V_2O_5, which is shown in Fig. 1, has a *Pmmn* orthorhombic

symmetry with 14 atoms per unit cell, and the experimental lattice parameters[21] $a = 11.512$ Å, $b = 3.564$ Å, and $c = 4.368$ Å. This reference crystal structure will be compared to less symmetric unit cells, where the atomic positions have been displaced, as detailed in Sec. III B. In all simulations we have used norm-conserving Troullier-Martins[50] pseudopotentials, including $3s$ and $3p$ semicore states for vanadium in the valence (total of 112 electrons), which have been already validated in previous studies on vanadates[51,52]. The KS ground-state calculation, in the local density approximation (LDA), converged with an energy cutoff of 100 Hartree and a $4 \times 4 \times 4$ **k**-point grid.

TDDFT calculations were performed within the RPA using 145 conduction and 41 valence bands. When comparing to the loss function calculated with the computationally more expensive BSE (Fig. 2) we have used $4 \times 4 \times 4$ **k**-point grid; for the comparison of the calculated loss function to experiment (Fig. 3) we have used a $6 \times 6 \times 6$ **k**-point grid, and a $8 \times 8 \times 8$ **k**-point grid to see the fine differences between the loss functions of ideal and distorted structures (Fig. 8). The **k**-point convergence study is reported in the Supplementary Material[53] (SM).

In the perturbative GW calculations, the dielectric matrix within a cutoff energy of 4.9 Hartree was computed within the RPA with LDA energies that were scissor-corrected to match the G_0W_0 band gap at the Γ point, using a $4 \times 4 \times 4$ **k**-point grid and 350 bands, while the self-energy required 700 bands and 52 Hartree cutoff energy.

The BSE spectra have been obtained with a $4 \times 4 \times 4$ **k**-point grid, with 15 valence and 16 conduction bands for absorption spectra (resulting in the converged spectra up to 7 eV), and 41 valence and 60 conduction bands for EELS spectra that were converged up to 23 eV. The BSE hamiltonian, Eq. (5), has been built, following the standard approach, using results from the perturbative GW calculations (with LDA wave functions and scissor corrected LDA energies) and a statically screened interaction W calculated in RPA with scissor-corrected LDA energies. In Ref.[54] the BSE hamiltonian for the ideal V_2O_5 crystal structure was built on the basis of an expensive QSGW calculation. The computational scheme employed here slightly reduces the exciton binding energy (e.g. from 1.0 eV to 0.8 eV in the case of the bright exciton, see first row of Tab. IV). However, most importantly, it gives the same physical picture of excitonic effects and makes the study at the same time meaningful and computationally feasible for the several distorted crystal structures analysed in the present work. More in general, all computational ingredients have been checked in this sense, where we could benefit from our results in Ref.[54], which contains a detailed analysis of the sensitivity of the absorption spectra with respect to the ingredients and computational choices in the BSE. We used this to set the frame which allows us in the present work to make comparisons that are significant, but obtained at a reasonable computational cost. App. A 1 and App. A 2 discuss in detail, respectively, the **k**-point convergence and the validity of the scissor correction approximation. A 0.15 eV Gaussian broadening was applied to the energy loss spectra and 0.1 eV to the absorption spectra. LDA and GW calculations were carried out with ABINIT[55], while the DP[56] and EXC codes[57] were used for TDDFT and BSE calculations, respectively.

III. RESULTS

A. Spectra of the ideal crystal

1. *Absorption spectra and exciton properties*

Absorption spectra of the ideal V_2O_5 crystal structure have been recently investigated in Ref.[54] by us. Here we summarize the main findings and we refer to Ref.[54] for a more extended discussion.

Our BSE calculations in Ref.[54] showed that the first peak at the onset of the absorption spectra is a tightly bound exciton, which is characterised by a large average electron-hole distance. The properties of this exciton are therefore in contrast with the textbook picture of the Frenkel exciton model, where a large exciton binding energy is associated with a strong localisation of the electron-hole pairs[3,58]. We explained this unusual behavior by means of a tight-binding model representing the charge transfer nature of the exciton that stems from electron-hole transitions within the V-O_b-V rungs having a mirror symmetry. The solution of the model gives an exciton wavefunction localised in the y and z directions but delocalised along x. Within the model, in this direction its extension is much larger than the V-O_b-V distance and does not depend on the strength of the electron-hole interaction.

The BSE calculation also revealed the presence of a pair of dark excitons (one for each V-O_b-V rung in the unit cell) below the onset of the optical spectrum. Even though they have a negligible dipole oscillator strength and therefore are not visible in the absorption spectrum, dark excitons play an important role in disexcitation processes like as phonon-assisted luminescence and light emission[59–61]. In V_2O_5 the dark excitons result from the same charge transfer transitions within the V-O_b-V rungs as the bright excitons at the optical onset and are described by the same tight binding model. These excitons are dark because of the destructive interference of single-particle transitions that are instead individually bright. Our tight-binding model showed that this is a consequence of the peculiar crystal symmetry of V_2O_5. Therefore, of particular interest here is what happens to the dark excitons when the structure is distorted and the symmetry broken.

2. Electron energy loss spectra

While Ref.[54] dealt with the exciton properties and the absorption spectrum of V_2O_5, here we also investigate its loss function. Its analysis provides a significant complementary viewpoint on the impact of local atomic distortions on many-body effects. Indeed, the loss function is dominated by plasmon excitations, which are usually associated with the long-range nature of the Coulomb interaction. Moreover, EELS allows for the study of the wavevector dependence of the electronic excitations, well beyond the dipole limit probed by optical spectroscopy.

The top panels of Fig. 2 compare the loss functions in the long-wavelength limit $-\mathrm{Im}\,\epsilon_M^{-1}(\mathbf{q}\to 0,\omega)$ calculated from the solution of the BSE with the spectra obtained within the GW independent-particle approximation (IPA) and the RPA of TDDFT. While in the latter the independent-particle energies in χ_0, see Eq. (1), are KS eigenvalues in the LDA, in the GW-IPA they are corrected by a rigid scissor that opens the band gap, simulating the GW corrections. The GW-IPA, however, completely neglects electron-hole interactions.

In comparison to the absorption spectra, excitonic effects are less prominent in the loss function. In the x and y directions, the GW-IPA spectra are mainly a blueshift of the RPA spectra, as an effect of the GW band-gap opening. Electron-hole interactions in the BSE have two main effects: they make the main peak at 11 eV broader, and they induce a redshift that partially compensates the difference between RPA and GW-IPA at the onset of the spectra. As a result of these cancellations, RPA spectra are much more similar to BSE than GW-IPA spectra. Most importantly, excitonic effects do not create new strong peaks within the band gap, since the dominant excitonic peaks in the absorption spectra are strongly renormalized, and become insignificant, in the EELS. In the z direction, besides those global shifts, a redistribution of spectral weight is also apparent between GW-IPA spectra on one side and RPA and BSE spectra on the other side. This is a manifestation of crystal local fields that will be analysed more in detail in the following. In any case, here we can already conclude that the main features in the loss function in V_2O_5 are adequately described at the level of the RPA, which will therefore also be adopted to investigate the dispersion of the loss function as a function of the momentum transfer.

From the analysis of the RPA and BSE loss functions in terms of the real and imaginary parts of the dielectric function shown in the middle and bottom panels of Fig. 2, we find that the 11 eV peak in the loss functions corresponds to a zero of $\epsilon_1(\mathbf{q}\to 0,\omega)$. Therefore it can be ascribed to a collective plasmon resonance rather than to an interband electron-hole excitation[62]. The spectral features at lower energies in the loss function are instead associated to peaks of $\epsilon_2(\mathbf{q}\to 0,\omega)$ and can therefore be considered to stem from interband transitions between the top-valence O $2p$ bands and the V split-off conduction bands. Finally, the very broad peak at larger energies around 23 eV matches a minimum of $\epsilon_1(\mathbf{q}\to 0,\omega)$, which however never crosses the zero axis. We can therefore assign it to a plasmon that is strongly damped by the interaction with single-particle excitations. While the plasmon at 11 eV is due to excitations of O $2p$ electrons into the V $3d$ empty bands, the broad plasmon at 23 eV is due to excitations to higher energy empty bands.

Fig. 3 shows the RPA loss function $-\mathrm{Im}\epsilon_M^{-1}(\mathbf{q},\omega)$ for several momentum transfers $\mathbf{q}$ along the 3 cartesian directions, calculated with or without the inclusion of local field effects (LFEs) over an extended energy range. The calculations are compared to the experimental EELS spectra of Ref. 62. For x and y directions, LFEs affect the spectra especially at large energies and have a stronger impact for increasing size of the momentum transfer. In the z direction, which is perpendicular to the V_2O_5 layers, the inhomogeneities are larger. Therefore, LFEs are much stronger, inducing essentially a blueshift of the spectra. As a result, the spectra along z are much more affected by LFE than the spectra along the in-plane x and y directions where the inhomogeneity is smaller. For the momentum transfers and in the whole energy range for which experimental results are available, the agreement with the calculated spectra is very good. Both the simulations and the experiment in the x and y directions display a main peak at $\sim$ 11 eV. The main peak is preceded by smaller spectral features and an onset located at $\sim$ 3 eV. All the peaks show little dispersion as a function of momentum transfer reflecting the localised character of the electronic excitations. The intensity of the main peak at $\sim$ 11 eV turns out to be systematically larger in the calculations than in the experiment. We note that that the momentum resolution in the EELS experiment[62] is as large as 0.05-0.06 Å^{-1}. Therefore, the resulting intensity of the measured peaks may have been strongly reduced in the experiment as a consequence of the angular integration. As a matter of fact, it is plausible that the experimental spectra for $\mathbf{q}$ along x and y in reality also contain contributions coming from the out-of-plane z direction, where at the same energy loss the calculated loss function does not display any intense feature. This also calls for further measurements with improved angular resolution, also for momentum transfers $\mathbf{q}$ along z, where experimental data are presently not available.

B. Effects of distortions

To study the impact of atomic displacements in V_2O_5 in detail, in the following we compare the spectra calculated in the ideal crystal structure with those obtained by slightly displacing the atoms of V_2O_5 inside the unit cell. The displacements we have chosen were inspired by related observations, in particular, phonon modes. However, it is important to stress that we do not claim that our distorted structures would correspond to crystals that are closer to realistic samples than the ideal

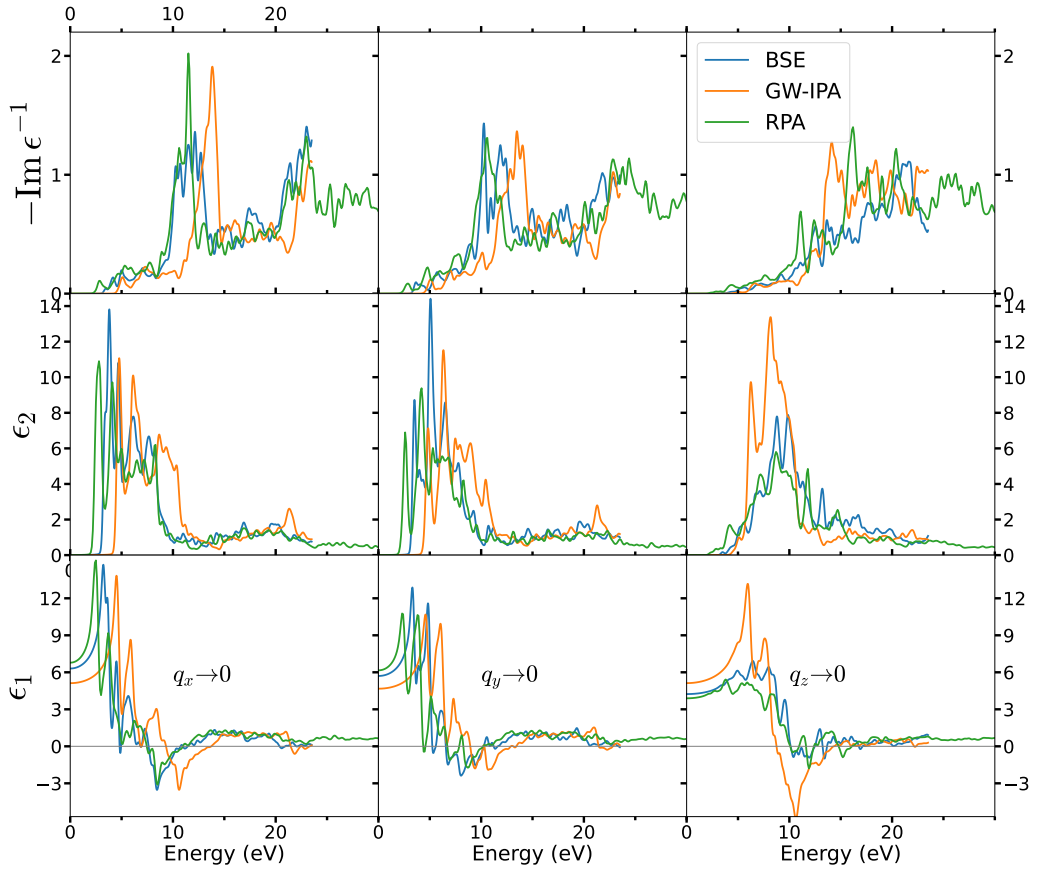

FIG. 2: Loss function $-\mathrm{Im}\epsilon_M^{-1}(\mathbf{q}\to 0,\omega)$ (top panels) and corresponding imaginary part $\epsilon_2(\mathbf{q}\to 0,\omega)$ (middle panels), and real part $\epsilon_1(\mathbf{q}\to 0,\omega)$ (bottom panels) of the macroscopic dielectric function of V_2O_5 in the 3 cartesian directions x (left), y (center) and z (right), computed within the TDDFT-RPA (green), the GW-IPA (orange) and the BSE (blue).

structure, not least because we keep the unit cell unchanged. Instead, they may be considered to be prototype distortions that allow us to analyse representative effects on absorption and loss function, both in view of the effects of distortions that are observed in applications based on nanostructured V_2O_5, and to draw general conclusions about the impact of local distortions in different kinds of spectroscopy.

1. *Away from the ideal crystal*

We consider deformations of the crystal structure of V_2O_5 from the experimental X-ray diffraction (XRD) positions[21] along the phonon modes calculated in Ref. 63. In the following, we show spectra obtained in the structures distorted along three representative vibrational modes: B^1_{1g}, B^5_{1u} and B^6_{2g}.

While the B^1_{1g} mode contains only displacements along the y direction, notably for V and O_v atoms, both the B^5_{1u} and B^6_{2g} modes contain x and z motions. In particular, the B^5_{1u} mode mainly corresponds to a stretch of the V-O_c bond, while B^6_{2g} is a V-O_b bond-stretch mode with a motion of the O_b atoms opposite to each other[63]. The phonon frequencies, ω_v, of these modes are: 147 cm^{-1} for B^1_{1g}, 963 cm^{-1} for B^6_{2g} (from Raman spectroscopy data)[64] and 570 cm^{-1} for B^5_{1u} (from infrared spectroscopy[65]). While these phonons except for B^1_{1g} are not contributing significantly to the thermal motion, they may still have an effect via the zero-point-motion electron-phonon coupling band gap and exciton renormalization. The characteristic length of a phonon mode v, $l_v = \sqrt{\hbar/2M\omega_v}$ is about 0.08 Å for the B^6_{2g} mode and 0.11 Å for the B^5_{1u} mode. (In the chosen modes, the maximum displacement corresponds to the O atom, so we used the O mass in these order of magnitude estimates.) These are comparable in magnitude to the arbitrarily chosen amplitudes here. However, beside possible zero-point motion corrections, within this work we are primarily concerned with the static local distortions, which may arise for various reasons, including sample preparation or nanostructuration. Therefore, within a reasonable range, the amplitudes of displacements are chosen arbitrarily conserving the relative motion of atoms along the corresponding phonon modes. For the B^5_{1u} and B^6_{2g} modes we have also considered a small and a large distortion (for each structure the largest displacements $d_{\max}$ are indicated in the first column of Tab. I). For the

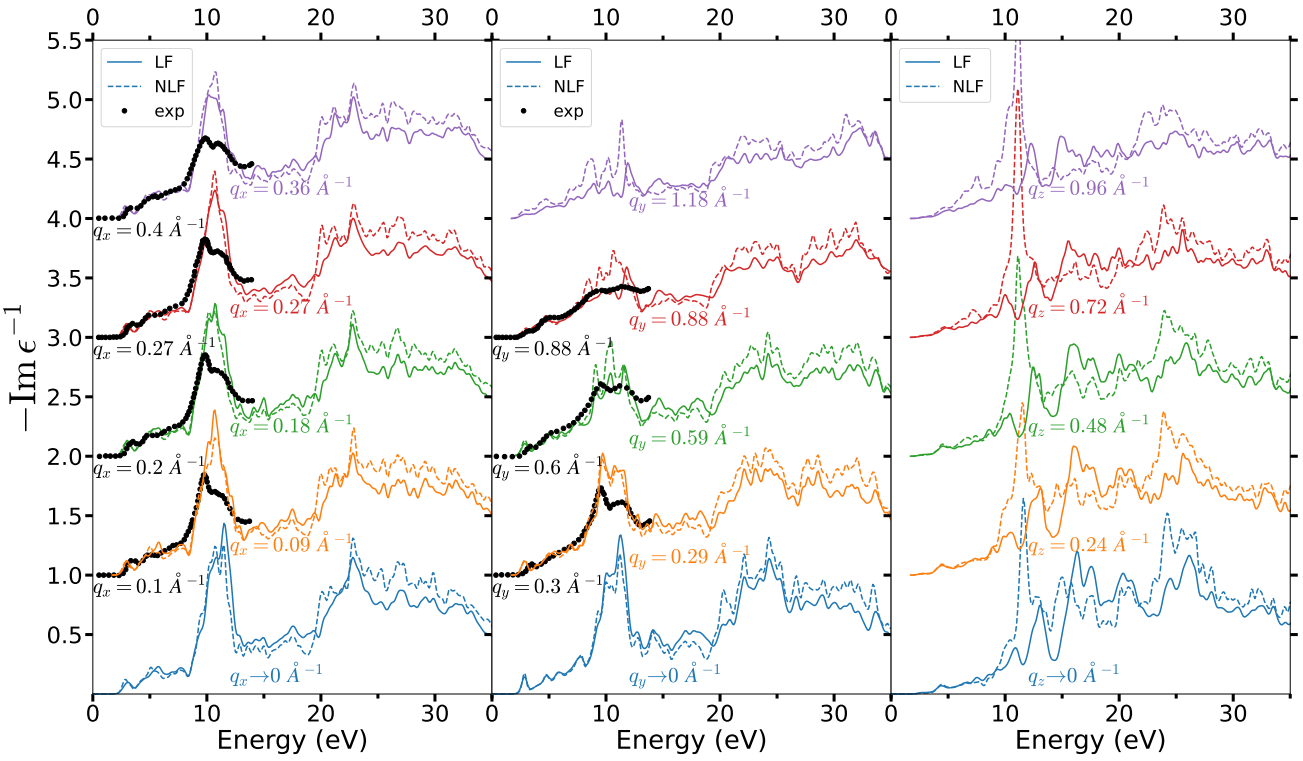

FIG. 3: Dispersion of the loss function $-\mathrm{Im}\epsilon_M^{-1}(\mathbf{q},\omega)$ as a function of momentum transfer $\mathbf{q}$ in the 3 cartesian directions, computed within TDDFT-RPA with (solid lines) and without (dashed lines) crystal local field effects, and comparison to EELS experimental data[62] (black dots). A vertical offset has been added to the spectra for improved clarity. The size of the theoretical or experimental momentum transfer is reported next to each spectrum.

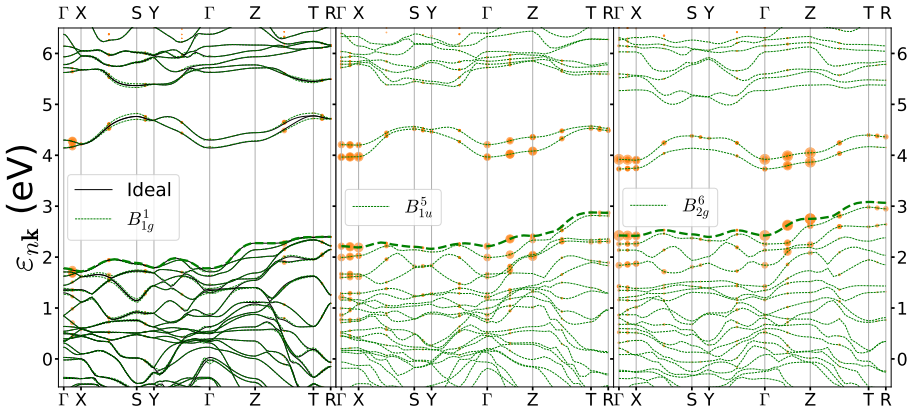

FIG. 4: LDA band structures of the ideal and distorted structures. The bold dashed lines indicate the top-valence band. The considered displacement corresponds to the largest one in Tab. I. The band structure of the crystal distorted along the B_{1g}^1 mode (left-most panel) almost entirely overlaps that of the ideal structure [see Fig. 1(c)]. The size of the orange circles is proportional to the contribution $|A_\lambda^{vc\mathbf{k}}\tilde{\rho}_{vc\mathbf{k}}|$ to the lowest energy exciton in the y polarization direction (see text).

distortions that we have examined in the present work, the bond length changes are reported in Tab. I. All the atomic positions of the deformed structures are listed in the SM[53]. The visualization of phonon modes can be found in Ref.[63].

2. *Effects of distortions on the band structure*

Fig. 4 shows the LDA band structures of the ideal and distorted structures in the regime of the largest atomic displacements. The LDA band gap[66] of the ideal structure is 1.8 eV. In the B_{1g}^1 case (left-most panel) the band structure almost entirely overlaps that of the ideal V_2O_5

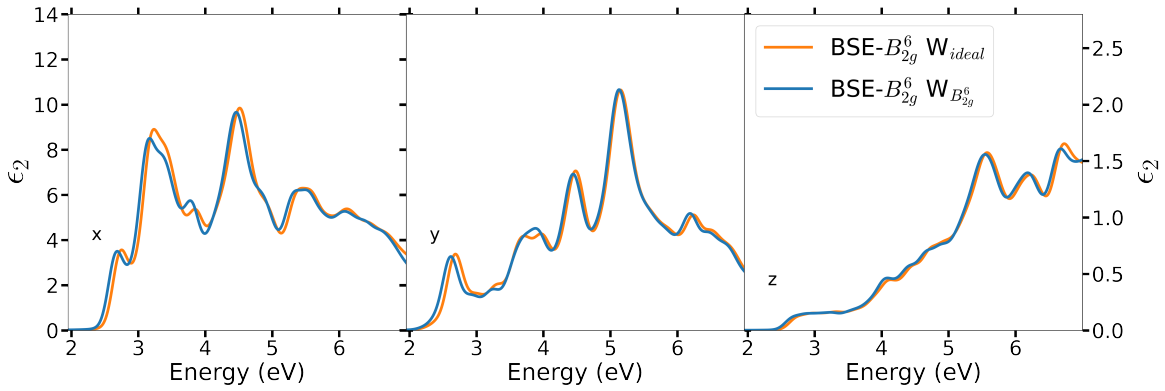

FIG. 5: The absorption spectra, in the 3 cartesian polarization directions, (left) x, (middle) y and (right) z, of the crystal structure distorted along the B^6_{2g} mode, for the case of the largest displacements using the BSE with W_{ideal} (orange lines) or the screened interaction W_{dist} of the distorted structure (blue lines).

Structure	V-O_b	V-O_{c2}	V-O_{c1}	V-O_{v1}
Ideal	1.78	2.02	1.88	1.58
B^1_{1g} $d_{max} = 0.03$ Å	1.78	2.02	1.86 1.89	1.58
B^5_{1u} $d_{max} = 0.02$ Å	1.77 1.79	1.99 2.05	1.88	1.58
B^5_{1u} $d_{max} = 0.12$ Å	1.72 1.84	1.85 2.19	1.87 1.89	1.58
B^6_{2g} $d_{max} = 0.04$ Å	1.72 1.83	2.02	1.88	1.58
B^6_{2g} $d_{max} = 0.13$ Å	1.63 1.92	2.00 2.04	1.88	1.57 1.59

TABLE I: Bond lengths of the ideal and distorted V_2O_5 structures (in Å). In the ideal structure, for each kind of bond, the length values are all the same. In the distorted structures, instead, they are not all equivalent anymore: the shortest and longest atomic distances for each kind of bond are therefore reported.

crystal. In all the other cases, instead, the band structure is strongly affected, with the band dispersions that are largely modified everywhere. As a consequence the LDA indirect band gap is reduced and goes from 1.74 eV for the B^1_{1g} to 1 eV for B^5_{1u} and 0.65 eV for B^6_{2g} case. The changes are the largest for the B^6_{2g} case (third panel in Fig. 4), where the two narrow bottom conduction bands are split everywhere across the Brillouin zone. The bands around the band gap therefore turn out to be very sensitive to the V-O_b bond stretch, distinctive of the B^6_{2g} phonon mode, and, to a smaller extent, to the V-O_c bond stretch, associated to B^5_{1u} phonon mode. They are instead quite stable with respect to displacements along y of the O_v atoms (B^1_{1g} mode). In the next section, we will examine how these modifications of the band structures due to the crystal deformations are reflected into changes of the optical properties.

3. *Absorption spectra of the distorted crystal*

For both GW and BSE calculations, an expensive part of the computation is the evaluation of the screened Coulomb interaction W. In principle, its calculation should be repeated for each of the different distorted structures. In Fig. 5 we analyse a possible shortcut for the BSE absorption spectra of the structure with the largest distortion for the B^6_{2g} mode. It is interesting to examine here this specific case more in detail since its band structure is the most affected by the crystal deformation.

In particular, we assess the possibility to employ the screened Coulomb interaction W_{ideal} of the ideal structure instead of W_{dist} of the distorted structure. The spectra remain very similar (compare blue and orange spectra): using W_{ideal} at the place of W_{dist} does not alter significantly the absorption spectra of the B^6_{2g} distorted structure. On the basis of these observations, we can conclude that we can safely calculate the absorption spectra of all the other distorted crystal structures (where the changes in the band structures are smaller than for the B^6_{2g} case) using the screened interaction W_{ideal} of the ideal crystal structure. We will analyse and explain these observations in detail in Sec. IV.

Fig. 6 compares the absorption spectra $\epsilon_2(\omega)$, calculated along the 3 cartesian polarization directions, for all distorted crystal structures to the spectra of the ideal V_2O_5. To examine how the excitonic properties of V_2O_5 change when the crystal structure is modified, we first consider the situations where the distortions along the phonon modes are small, with the largest displacements between $d_{\text{max}} \sim 0.02$ Å and $d_{\text{max}} \sim 0.04$ Å. While the B^1_{1g} mode has a negligible effect on the spectra, for the B^5_{1u} mode and especially the B^6_{2g} mode the changes are sizable in all directions (compare gray and blue lines in Fig. 6). For the larger crystal distortions along the B^5_{1u} and B^6_{2g} phonon modes, there are conspicuous changes in the spectra (compare gray and orange solid lines in Fig. 6): the energy of the first bright exciton is redshifted by up to 0.7 eV and the shape of the lowest energy peaks is strongly modified.

By comparing the GW-IPA spectra (dashed lines), we observe that the effects of the distortions are already

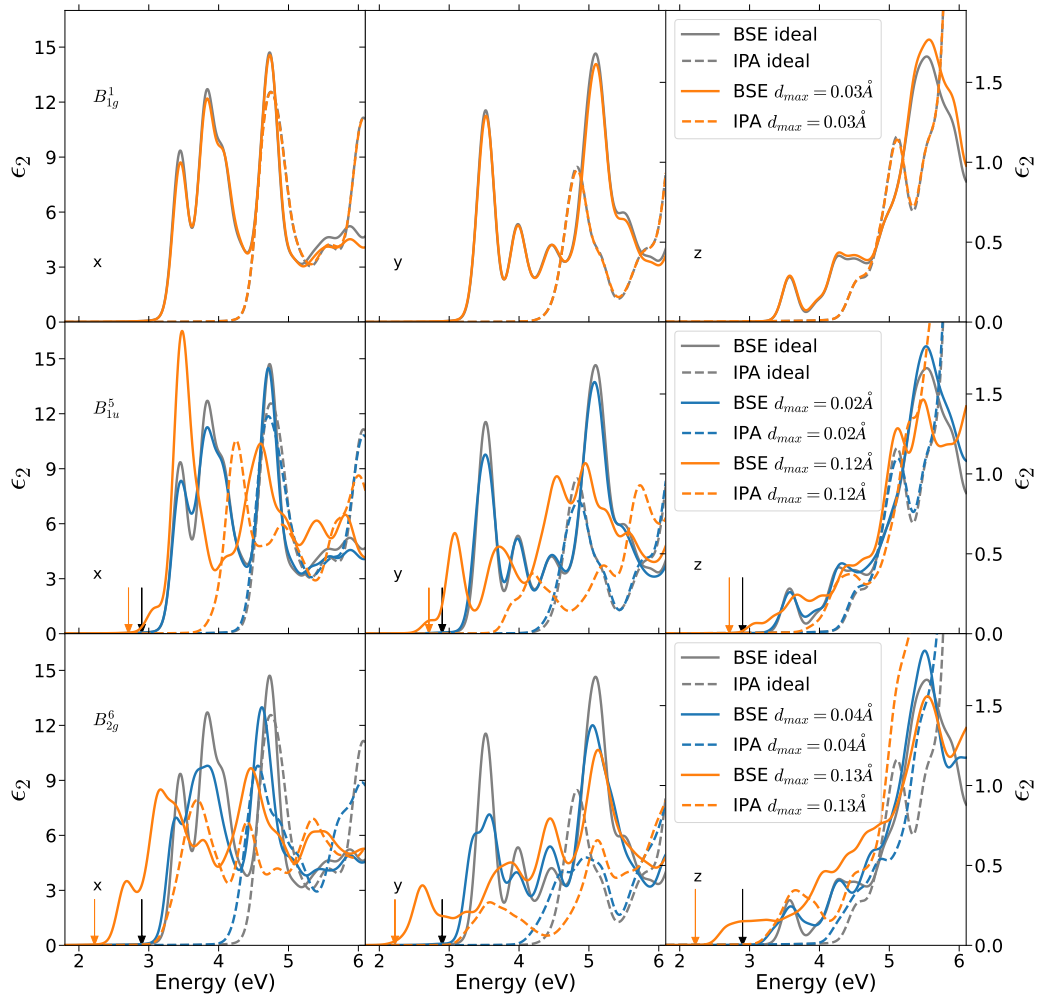

FIG. 6: Absorption spectra of the distorted crystal structures (orange and blue lines) compared to the absorption spectra in the V_2O_5 ideal structure (gray lines). The spectra are obtained from the solution of the BSE (solid lines) and from the GW-IPA (dashed lines), where e-h interactions are neglected. The d_{max} values are the largest atomic displacement in the unit cell with respect to the ideal crystal (see Tab. I). For the B^5_{1u} and B^6_{2g} phonon modes both a small (blue lines) and large (orange lines) displacement are considered. The arrows for the structures distorted along the B^6_{2g} and B^5_{1u} modes indicate the lowest exciton energy, which is perfectly dark in the ideal V_2O_5 structure (black arrows), but not in the y direction in the distorted structures (orange arrows).

largely visible: the BSE spectra (solid lines) actually follow the same trends of the GW spectra. The redshifts of the energies of the first bright excitons, see Tab. II, are the combined effect of two changes: the shrinkage of the GW direct band gap and the reduction of the exciton binding energy. We find that the band gap change gives the largest contribution to the spectral redshift, while the binding energies of both the lowest energy bright and dark excitons remain comparatively more stable. We will analyse the origin of these changes more in detail in Sec. IV.

For the B^5_{1u} and B^6_{2g} modes, the BSE spectra (orange solid lines) in the y direction also develop a tail on the low energy side of the first prominent peak (see orange arrows). This points to the fact that the lowest energy exciton that is perfectly dark in the ideal V_2O_5 structure (see black arrows) has some non-vanishing oscillator strength in the y direction in these distorted structures.

This lowest energy exciton in the y-polarization shifts to 2.3 and to 2.7 eV when applying the B^6_{2g} and B^5_{1u} phonon distortions respectively. The ϵ_2 for these two excitons is about 25 and 13 times smaller than for the first bright exciton in this polarization for the perfect crystal, and this is for phonon amplitudes that are still somewhat larger than our estimate of the corresponding phonon length scale $l_{B^6_{2g}}$ and $l_{B^5_{1u}}$ from zero-point-motion. However, this is still compatible with the 2 orders of magnitude lower absorption at the 2.3 eV onset than for the bright exciton near 3 eV. in Ref. 67. Thus, the often quoted lower band gap extracted from the onset

Structure	Optical onset	Direct bandgap	E_b bright	E_b dark
Ideal	3.4	4.2	0.8	1.3
B^1_{1g} $d_{max} = 0.03$ Å	3.4	4.2	0.8	1.3
B^5_{1u} $d_{max} = 0.023$ Å	3.4	4.2	0.8	
B^5_{1u} $d_{max} = 0.12$ Å	3.1	3.8	0.7	1.1
B^6_{2g} $d_{max} = 0.04$ Å	3.4	4.1	0.7	
B^6_{2g} $d_{max} = 0.13$ Å	2.7	3.3	0.6	1

TABLE II: Energy of the first bright exciton (termed "Optical onset") for x polarization from BSE calculation, smallest direct band gap from scissor-corrected LDA and exciton binding energy (in eV) of the lowest energy bright and dark excitons for the ideal and distorted V_2O_5 structures.

of absorption could plausibly be ascribed to brightening of the dark exciton by zero-point motion electron-phonon renormalization of the exciton. While this is clearly not a complete calculation of the exciton-phonon coupling effect, it is still a plausible reason for the lower onset of absorption near 2.3 eV. Alternatively, indirect band gap excitons could also contribute again by electron phonon coupling.

4. *Brightening of the dark excitons*

The oscillator strength of each exciton λ is given in Eq. (6) by the square modulus of the sum over transitions $v\mathbf{k} \to c\mathbf{k}$ of the products $A^{vc\mathbf{k}}_\lambda \tilde{\rho}_{vc\mathbf{k}}$. Therefore, in order to understand how the dark exciton of the ideal V_2O_5 structure becomes bright for the y polarization direction in the crystal structures distorted along the B^5_{1u} and B^6_{2g} modes, we analyse the contributions $A^{vc\mathbf{k}}_\lambda \tilde{\rho}_{vc\mathbf{k}}$ to the exciton oscillator strength. As shown in Ref.[54], in the ideal crystal structure the dark exciton is the result of the destructive interference of contributions $A^{vc\mathbf{k}}_\lambda \tilde{\rho}_{vc\mathbf{k}}$ stemming from $\mathbf{k}$ points that are equivalent by symmetry, each term $A^{vc\mathbf{k}}_\lambda \tilde{\rho}_{vc\mathbf{k}}$ being separately different from zero. Fig. 4 represents the individual contribution $|A^{vc\mathbf{k}}_\lambda \tilde{\rho}_{vc\mathbf{k}}|$ in the band structure plot for the distorted V_2O_5 structures. There we consider specifically the y polarization of matrix elements for the lowest energy exciton. Each transition $v\mathbf{k} \to c\mathbf{k}$ is represented by a pair of orange circles, one in a valence band and the other in a conduction band, at the same $\mathbf{k}$ point. The size of the circle is proportional to the weight of each contribution. We find that there are many contributions different from zero, mainly involving the top-valence and bottom-conduction bands. The B^1_{1g} structure (left-most panel in Fig. 4), where the exciton remains dark, is the closest to the ideal structure. In particular, it preserves the inversion symmetry. The B^5_{1u} and B^6_{2g} distorted structures (see second and third panels Fig. 4), instead, only preserve the m_y reflection symmetry with respect to the y axis. In these two distorted structures the individual contributions $|A^{vc\mathbf{k}}_\lambda \tilde{\rho}_{vc\mathbf{k}}|$

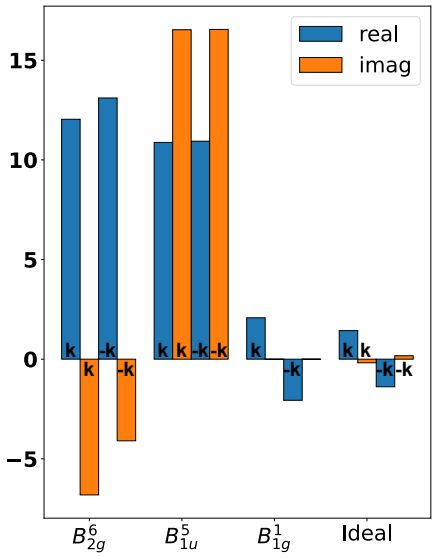

FIG. 7: Contributions to the oscillator strength of the lowest energy exciton in the y polarization direction for the crystal structures distorted along B^6_{2g} (first histograms from the left), B^5_{1u} (second histograms), B^1_{1g} (third histograms) modes in comparison to the ideal V_2O_5 case (fourth histograms). Blue (orange) columns represent the real (imaginary) parts of $\sum_{vc\mathbf{k}} A^{vc\mathbf{k}}_\lambda \tilde{\rho}_{vc\mathbf{k}}$, where the sum over $\mathbf{k}$ is restricted to one half of the first Brillouin zone. The $\mathbf{k}$ points belonging to each subset are related to those of the other subset by inversion symmetry $\mathbf{k} \leftrightarrow -\mathbf{k}$. In the B^1_{1g} and ideal structures, the columns have same heights but opposite signs, so the exciton is dark. In the other distorted structures, the columns are higher and their signs do not cancel, so the exciton becomes bright.

become larger than in the ideal case and, in addition, stem from high-symmetry $\mathbf{k}$ points (e.g. X, Z, T and Γ). Notably, in the ideal and B^1_{1g} structures $|A^{vc\mathbf{k}}_\lambda \tilde{\rho}_{vc\mathbf{k}}|$ is zero at the Γ point, which is not equivalent by symmetry to other $\mathbf{k}$ points in the first Brillouin zone. Interestingly, in x direction, instead, the corresponding $|A^{vc\mathbf{k}}_\lambda \tilde{\rho}_{vc\mathbf{k}}|$ in the distorted crystal structure remain similar to the ideal case and come from the same part of the Brillouin zone (see SM[53]).

To illustrate the cancellation, associated with the inversion symmetry $\mathbf{k} \to -\mathbf{k}$, of the individual contributions in the resulting absorption spectrum, we have divided the Brillouin zone in two half volumes, either containing a $\mathbf{k}$ point or its corresponding $-\mathbf{k}$. We have then restricted the sum over $\mathbf{k}$ points in Eq. (6) to either half of the Brillouin zone. In the ideal crystal structure, the two semi-sums are small, but still different from zero (see the rightmost histograms in Fig. 7). However, they are equal and with an opposite sign, which implies that they cancel when summed together, giving rise to the dark exciton with negligible oscillator strength. This holds true also for the B^1_{1g} case, whereas in the B^6_{2g} and B^5_{1u} dis-

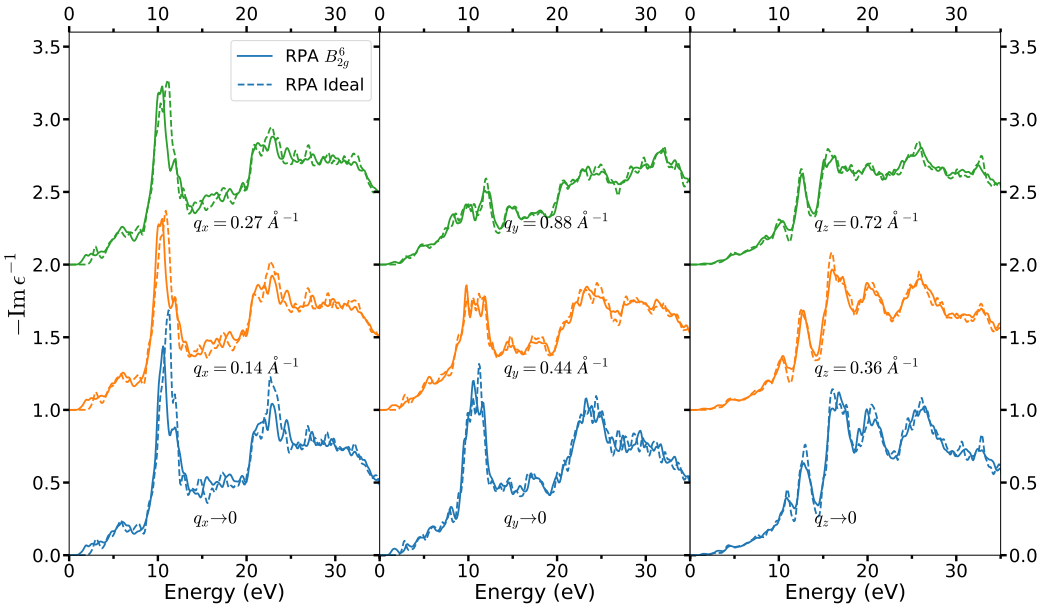

FIG. 8: TDDFT-RPA loss function spectra $-\mathrm{Im}\epsilon_M^{-1}(\mathbf{q},\omega)$ as a function of the momentum transfer $\mathbf{q}$ along the x (left), y (middle) and z (right) directions, calculated for the structure distorted along the B_{2g}^6 mode (solid lines) and the undistorted structure (dashed lines). A vertical offset has been added to the spectra for improved clarity. The size of the momentum transfer is reported next to each spectrum

torted structures (see two leftmost histograms in Fig. 7) the semi-sums have much larger intensities, and, most importantly, they have the same sign. As a result, in these distorted structures the dark exciton becomes visible at the onset of the absorption spectra. In particular, for the B_{1u}^5 structure the real and imaginary parts have the largest intensity, which also explains why the corresponding peak has a larger intensity in the spectrum.

5. *Electron energy loss spectra of the distorted crystal*

Fig. 8 shows the RPA loss functions for several momentum transfers along the 3 cartesian directions calculated in the structure distorted along the B_{2g}^6 mode, where the effect on the absorption spectrum is the largest. These loss functions are compared to the corresponding spectra calculated in the ideal V_2O_5 crystal structure. For all the momentum transfers, the spectra of the distorted structure remain very similar to the ideal case. In particular, the plasmon resonances at 11 and 23 eV are not strongly affected by the local distortions: we observe a small redshift by 0.5 eV and a minor reduction of intensity of the peaks. The largest modifications occur in the low-energy region, for $\omega < 10$ eV, where the peaks with lower intensity are associated to spectral features ϵ_2 and therefore undergo similar changes as in the absorption spectra. In other words, while the absorption spectra are largely modified by the structural distortions, mainly through changes in the underlying band structure, the loss function spectra are much more stable. We can understand this striking difference between the two excitation spectra by the fact that plasmons are collective excitations of the electronic charge that are mainly linked to properties of the global environment like the average electron density and are much less sensitive to changes of bond lengths. In the next section, we will therefore analyse more in detail the origin of the changes in the absorption spectra.

IV. DISCUSSION

Our main focus of interest here is to analyze the effect of structural distortions on the many-body effects in the spectra. We consider in particular the representative case of the structure distorted according to the B_{2g}^6 mode with the larger atomic displacement of 0.13 Å.

A. Screening in the short- and long-range

On the level of the GW approximation, the effective interaction entering both the self-energy and the electron-hole interaction is the screened Coulomb interaction W. The computation of the screening is the most expensive part of the calculations, and at the same time, the interpretation of changes in screening upon changes in the material is not straightforward. It is therefore worthwhile to examine it more in detail. Fig. 9 shows the static macroscopic dielectric constant $\epsilon_M(\mathbf{q},\omega=0)$, defined in Eq. (3), that screens the Coulomb interaction in momentum space. ϵ_M takes different values for the same

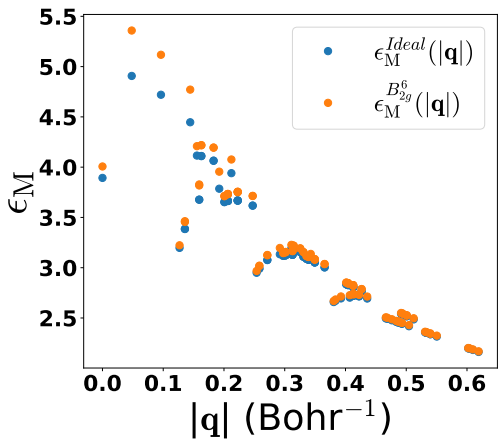

FIG. 9: Static macroscopic dielectric function $\epsilon_M(\mathbf{q},\omega=0) = 1/\epsilon^{-1}_{\mathbf{G}=0,\mathbf{G}'=0}(\mathbf{q},\omega=0)$ for ideal and distorted structures (blue and orange dots, respectively) calculated within the RPA. The values at $|\mathbf{q}| \to 0$ have been calculated along the direction (1,2,3) in reciprocal lattice units and are meant to represent an average of the different spatial directions.

or similar $|\mathbf{q}|$; this is due to the inhomogeneity and the anisotropy of V_2O_5. Especially the anisotropy explains the peculiar shape of the distribution, since the screening perpendicular to the planes is significantly weaker than the in-plane screening. As one would expect, at large $|\mathbf{q}|$, where short distances are probed, any dielectric function tends to 1 and therefore the distorted and undistorted systems give similar values. Moreover, the dependence on the direction of $\mathbf{q}$ is weak. At smaller $\mathbf{q}$ screening increases, and with this, a stronger direction dependence arises and distorted and undistorted results start to differ. This is particularly clear between 0.2 and 0.05 Bohr^{-1}. The curve seems to drop at $\mathbf{q} \to 0$, but this is merely due to the fact that we show here a particular direction of $\mathbf{q}$, namely (1,2,3) in reciprocal lattice units. The figure suggests that results will be most affected by the changes in screening upon distortion when they are dominated by smaller $\mathbf{q}$, hence, by larger distances. It is therefore interesting to analyse the role of distortions in the GW and BSE results.

B. Consequences of the screening

1. *In the GW quasiparticle corrections*

The changes in the GW QP corrections - see Eq. (4) - can come through changes of the wavefunctions used in the calculations of matrix elements, changes of Kohn-Sham energies in the one-body Green's function, and the changes of the screening observed above. In Tab. III we first compare the main matrix elements at the Γ point that result from the GW calculation for the top valence (tv) and bottom conduction (bc) states, for the ideal and distorted structures, see rows ① and ②, respectively. In the table, the GW matrix elements are broken up into the different contributions adding up in Eq. (4), which we analyse separately.

In the third column, the KS energies $\varepsilon_{n\mathbf{k}}$ are given, with the noteworthy distortion-induced changes consistent with the band structure in Fig. 4. The bare exchange matrix elements $\langle\Sigma_x\rangle$, which depend only on wave functions, are shown in the fifth column. The distortions lead to an upshift of the valence band and a downshift of the conduction band by about 0.2 eV, which represents only 1 and 2% of $\langle\Sigma_x\rangle$ for the valence and conduction state, respectively. The increased exchange of the conduction state points to an on average stronger overlap of conduction and valence states upon distortion, which may stem from a slight average delocalization of the valence state that would explain its reduced exchange matrix element. Screening enters the correlation contribution $\langle\Sigma_c(\varepsilon_{n\mathbf{k}})\rangle$ to the self-energy in the sixth column. This contribution can be split into an overall downwards shift due to the short-range Coulomb hole, and a contribution that reduces the exchange downshift, i.e., an upshift, which is dominant for the valence band where exchange is stronger. The cancellations result in a correlation contribution that exhibits changes of similar magnitude as the bare exchange, in spite of the changed screening. The energy dependence of the self-energy, measured by the quasiparticle renormalization factor $Z_{n\mathbf{k}}$ in the seventh column, is marginally affected. The resulting total self-energy matrix element of the conduction state does not reflect any significant changes upon distortion, whereas the valence band self-energy changes by about half an eV. However, the matrix elements of the KS potential $\langle V_{xc}\rangle$ in the forth column show the very same trends, which means that the final quasiparticle correction $E_{n\mathbf{k}} - \varepsilon_{n\mathbf{k}}$ changes by less than 0.1 eV. It is very important to stress that there is indeed a noteworthy change of the valence band energy due to changes in the xc effects upon distortions, but that this change is already captured by the Kohn-Sham potential.

The main computational effort in the GW calculation is the evaluation of screening. The row ③ of Table III shows the results obtained using the distorted structure, but with W_{ideal} computed in the ideal crystal. Being able to use W_{ideal} throughout would indeed constitute a significant computational gain. Therefore, we now compare rows ② and ③. In order to evaluate directly the quality of the approximation, one has to check the matrix element of the correlation self-energy $\langle\Sigma_c(\varepsilon_{n\mathbf{k}})\rangle$ in the sixth column of Table III. The calculation using the W_{ideal} captures about 70% of the effect of distortion on the valence band, whereas it overestimates the distortion effects by about 50% on the conduction band. In other words, the distortion effects are captured to a significant extent, though not with high precision. It should be noted, however, that the differences here are of the order of 0.1-0.2 eV, which starts to be in the range of the precision of the GW calculation itself. Moreover, as pointed out above,

Structure	Band	$\varepsilon_{n\mathbf{k}}$	$\langle V_{\rm xc}\rangle$	$\langle\Sigma_{\rm x}\rangle$	$\langle\Sigma_{\rm c}(\varepsilon_{n\mathbf{k}})\rangle$	$Z_{n\mathbf{k}}$	$E_{n\mathbf{k}}-\varepsilon_{n\mathbf{k}}$	$E_{n\mathbf{k}}$
① Ideal	tv	1.78	-19.88	-24.24	4.02	0.78	-0.27	1.51
	bc	4.14	-22.30	-14.22	-5.57	0.77	1.95	6.09
② Distorted (with $W_{\rm dist}$)	tv	2.42	-19.51	-23.97	4.23	0.77	-0.17	2.25
	bc	3.73	-22.34	-14.41	-5.40	0.77	1.95	5.68
③ Distorted (with $W_{\rm ideal}$)	tv	2.42	-19.51	-23.97	4.16	0.77	-0.22	2.20
	bc	3.73	-22.34	-14.41	-5.32	0.77	2.02	5.75

TABLE III: Individual contributions to the GW QP corrections - see Eq. (4) - for the top-valence (tv) and bottom conduction (bc) bands at $\mathbf{k}=\Gamma$ for the ideal V_2O_5 and the crystal structure distorted along the B_{2g}^6 mode with largest atomic displacement $d_{\rm max}=0.13$ Å. For the distorted structure two calculations are compared: using the screened Coulomb interaction W calculated either in the distorted structure $W_{\rm dist}$ (second row) or in the ideal structure $W_{\rm ideal}$ (third row).

the final QP correction $E_{n\mathbf{k}}-\varepsilon_{n\mathbf{k}}$ is very well described even by a fully ideal calculation, thanks to the fact that the effects of distortion is already well captured in the Kohn-Sham calculation.

2. *In the BSE calculations*

In the BSE calculation of the exciton the e-h interaction has no Kohn-Sham counterpart, and one would therefore not expect cancellations. This would mean that distortions could lead to major changes and require a recalculation of W. Indeed, the optical gaps and exciton binding energies in Table II show that distortions can induce significant changes. The distortion of 0.13 Å along the B_{2g}^6 mode leads to a 0.9 eV decrease of the direct band gap at the Γ point: it is accompanied by a decrease of the energy of the first bright exciton of 0.7 eV, which means, the binding energy of the bright exciton decreases by 0.2 eV, from 0.8 to 0.6 eV. The binding energy of the dark exciton shows a similar decrease of 0.3 eV. This is a relatively moderate change of the binding energy, and one might want to conclude quickly that the excitons do not feel the distortion strongly.

However, a closer look incites to be cautious. We first consider the matrix elements of W calculated using the exciton wavefunction in a state λ:

$$\langle W_\lambda\rangle \;=\; \sum_{\substack{vc\mathbf{k}\\ v'c'\mathbf{k}'}} A_\lambda^{*vc\mathbf{k}}\langle vc\mathbf{k}|W|v'c'\mathbf{k}'\rangle A_\lambda^{v'c'\mathbf{k}'}\,. \qquad (7)$$

The rows and columns of Tab. IV identify the possible choices, respectively, for the eigenvectors $A_\lambda^{vc\mathbf{k}}$ and the matrix elements $\langle vc\mathbf{k}|W|v'c'\mathbf{k}'\rangle$ that enter Eq. (7). In the row ①, the expectation value (7) is calculated using the eigenvectors $A_\lambda^{vc\mathbf{k}}$, for the bright and dark excitons, obtained from the excitonic hamiltonian of the ideal structure. In the row ②, instead, the excitonic eigenvectors $A_\lambda^{vc\mathbf{k}}$ are calculated in the distorted structure (where the excitonic hamiltonian contains a screened interaction W that is also calculated in the distorted structure). In third column, named $\langle W_\lambda\rangle_{\rm ideal}$, the matrix elements $\langle vc\mathbf{k}|W|v'c'\mathbf{k}'\rangle$ of the screened Coulomb interaction calculated in the ideal structure enter Eq. (7). In the forth column $\langle W_\lambda\rangle_{\rm dist}$, instead, they are the matrix elements $\langle vc\mathbf{k}|W|v'c'\mathbf{k}'\rangle$ calculated in the distorted structure.

Structure	Exciton	$\langle W_\lambda\rangle_{\rm ideal}$	$\langle W_\lambda\rangle_{\rm dist}$	$E_\lambda^{\rm eff}$	$E_{\rm g}$	E_b
① Ideal	Dark	1.9		4.7	4.2	1.3
	Bright	1.7		5.0		0.8
② Distorted	Dark	1.6	1.6	3.7	3.2	1
	Bright	1.0	1.0	3.5		0.6
③ Distorted (with $W_{\rm ideal}$)	Dark	1.6	1.6	3.9	3.3	1
	Bright	1.0	1.0	3.6		0.6

TABLE IV: Matrix elements (in eV) of the screened Coulomb interaction, see Eq. (7), in the ideal and distorted crystal structures ($\langle W_\lambda\rangle_{\rm ideal}$ and $\langle W_\lambda\rangle_{\rm dist}$, third and forth columns, respectively), and the effective gap $E_\lambda^{\rm eff}$ (fifth column), see Eq. (8)„ calculated using the exciton wavefunctions obtained in the ideal and distorted structures (second and third rows, respectively), for the dark and bright excitons. The fifth an sixth columns report the gaps and the exciton binding energies. In the bottom row, the exciton wavefunctions are obtained in the distorted crystal structure using in the BSE hamiltonian the screened interaction $W_{\rm ideal}$ from the ideal structure.

We first consider the difference $\langle W_\lambda\rangle_{\rm ideal}$-$\langle W_\lambda\rangle_{\rm dist}$ between rows ① and ②. This expectation value difference should give a rough estimate of the change of exciton binding energy, and indeed, in the case of the dark exciton the distortion decreases $\langle W_\lambda\rangle$ from 1.9 to 1.6 eV, i.e., by 0.3 eV, right the decrease from 1.3 to 1.0 eV of the binding energy E_b (see last column of Tab. IV). However, the same is not true for the bright exciton: here $\langle W_\lambda\rangle$ decreases as much as 0.7 eV (from 1.7 to 1.0 eV), which is almost four times the 0.2 eV decrease of the binding energy. This indicates that there is a significant change in the bright exciton wave function $A_\lambda^{vc\mathbf{k}}$, although this cannot be detected in its binding energy.

Tab. IV also compares $\langle W_\lambda\rangle$ from Eq. (7) with the direct gap E_g (sixth column) and the effective gap $E_\lambda^{\rm eff}$ (fifth column), defined as:

$$E_\lambda^{\rm eff} = \sum_{vc\mathbf{k}} |A_\lambda^{vc\mathbf{k}}|^2 (E_{c\mathbf{k}}-E_{v\mathbf{k}})\,, \qquad (8)$$

i.e., the expectation value of the conduction-valence energy difference in the excitonic state of interest. Indeed, neglecting the weak local field effects, the exciton binding

energy is given by:

$$E_b = E_g - \left(E_\lambda^{\text{eff}} - \langle W_\lambda \rangle\right), \tag{9}$$

rather than by $\langle W_\lambda \rangle$ alone. Even for our low-lying excitons, the difference between the minimum direct gap E_g and the effective gap E_λ^{eff} can be significant: it is 0.8 eV for the bright exciton in the ideal structure, as the row ① of Table IV shows. In order to understand the change in binding energy upon distortion, we therefore also have to examine the change of effective gap.

The distortion decreases both E_g and E_λ^{eff} of the dark exciton by 1 eV (compare rows ① and ②), meaning that the change in binding energy E_b of the dark exciton is indeed due to a change in $\langle W_\lambda \rangle$ [see Eq. (9)]. E_λ^{eff} of the bright exciton, instead, decreases by as much as 1.5 eV, which cancels to a large extent the 0.7 eV decrease of the bright $\langle W_\lambda \rangle$, leading to a similar change in binding energy as for the dark exciton, but with a different interpretation: visibly, the nature of the bright exciton is significantly affected by the distortion.

Again, it is interesting to examine whether this change is due to a change of screening. Table IV therefore compares $\langle W_\lambda \rangle$, see Eq. (7), calculated by using the matrix elements $\langle vc\mathbf{k}|W|v'c'\mathbf{k}'\rangle$ in the ideal (third column) or the distorted (forth column) structure. For the exciton wavefunction $A_\lambda^{vc\mathbf{k}}$, in Eq. (7) we also use the result of the excitonic Hamiltonian constructed with the QP electronic structure of the distorted system and with either the screened interaction W_{dist} of the distorted structure (row ②) or W_{ideal} of the ideal structure (row ③). All the four possible combinations entering Eq. (7) always give the same results, both for bright and dark excitons, meaning that the choice of W has almost no consequences, neither in the excitonic hamiltonian nor in Eq. (7).

We can conclude this part by noting that the change of $W(\mathbf{r}, \mathbf{r}')$ due to distortion has negligible impact on the exciton and can safely be neglected, confirming that one can use the screened Coulomb interaction calculated in the ideal system. This stability is even more pronounced than in the case of the self-energy, maybe due to the fact that the exciton probes shorter distances. This suggests that when studying bound excitons in systems with defects, disorder and at finite temperature, the screened Coulomb interaction of the ideal structure can be used, which will increase the feasibility of such studies[68,69].

The change in the QP energies and wavefunctions upon distortion, instead, changes the exciton wavefunction and therefore the effective gap and the matrix element of W, with an effect on the exciton binding energy that is very much reduced thanks to a cancellation between the two changes. The fact that the exciton wavefunction changes under the distortion can be directly appreciated in Fig. 10: both the dark and the bright exciton have a tendency to decrease their extension in x direction and increase in y direction, with the distorted distribution of the electron being non-symmetric with respect to the position of the hole due to non-symmetric V-O_b-V bond lengths. Examining the exciton mean radius over the supercell volume Ω for each direction $\alpha = \{x, y, z\}$

$$\langle |r_\lambda^\alpha| \rangle = \frac{1}{\Omega} \int_\Omega d\mathbf{r}_e |r_e^\alpha - r_h^{0\alpha}| |\Psi_\lambda(\mathbf{r}_h^0, \mathbf{r}_e)|^2$$

can give a quantitative estimate of the localisation character of the exciton. For the ideal structure the exciton radii of the dark and bright excitons form an ellipsoid with axes: (5.3, 2.0, 2.8)Å and (8.8, 3.3, 4.0)Å, respectively. In the distorted structure they become (4.7, 2.2, 3.3)Å and (7.8, 3.3, 3.9)Å, respectively. Although these effective radii show that the change is less dramatic than what the picture would maybe suggest, the effect is still sizeable and one should be aware of it and not judge on the absence of changes by just looking at the binding energy.

V. CONCLUSIONS

We have analysed the electron excitation spectra of V_2O_5 and investigated in detail the different impact of structural deformations on the optical and dielectric properties of V_2O_5. While excitons in optical absorption spectra are sensitive to the local atomic environment, especially through modifications of the band structure, plasmons in loss function spectra see mainly the global environment and are less affected by local distortions. In particular, we have shown that the modifications in the optical spectra are due to counteracting changes. The impact of the structural distortion on the effect the electron-electron interaction on the band structure is the result of cancellations, to a very large extent, between the changes of the GW self-energy and of the Kohn-Sham xc potential. As a result, the main effect of the distortion is already captured at the level of the Kohn-Sham band structure. Similarly, the change in the effective band gap largely compensates the change in the electron-hole interaction in the BSE exciton hamiltonian. As a result the exciton binding energy turns out to be less affected, even though the nature of the exciton can be significantly impacted by the local distortion. Finally, our results show that, and why, for the simulation of excitons in materials with low-symmetry crystal structures, or in presence of disorder, the screened Coulomb interaction of a higher-symmetry structure can be used, promising a large computational gain.

ACKNOWLEDGEMENTS

We thank Claudia Rödl for suggesting us to look into the particular convergence of the BSE JDOS and absorption spectra, and for insightful discussions. This work benefited from the support of EDF in the framework of the research and teaching Chair "Sustainable energies" at Ecole Polytechnique. Computational time was granted by GENCI (Project No. 544). WRLL was supported

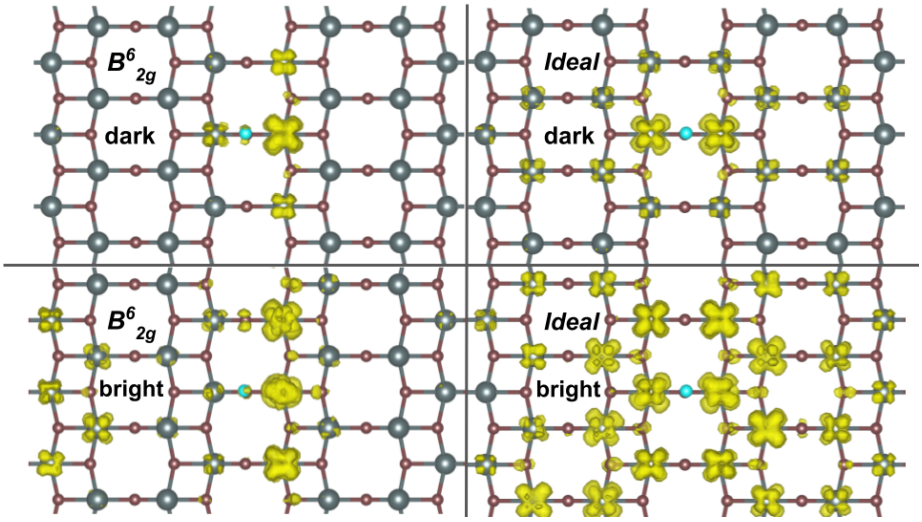

FIG. 10: Spatial distribution of the wavefunction $|\Psi_\lambda(\mathbf{r}_h, \mathbf{r}_e)|^2$ of the lowest energy dark (upper panels) and bright excitons in y polarization (bottom panels) for fixed position of the hole $\mathbf{r}_h^0$ close to a bridge oxygen O_b atom (light blue dot): distorted crystal structure along the B_{2g}^6 mode (left panels) and ideal crystal structure (right panels). The isosurface value corresponds to 2% of the maximum.

by the US Department of Energy-Basic Energy Sciences under grant No. DE-SC0008933.

Appendix A: Additional computational information

It is useful to look closer to two aspects of the calculations in order to combine efficiency and accuracy.

1. k-point convergence

It is important to note that the precision required depends very much on the feature of interest. The convergence with the **k**-point grid is a particularly good example for this point, and since it has not been treated exhaustively in Ref.[54], we will give details here. The upper panel of Fig. 11 shows the **k**-point grid convergence of the absorption spectrum in the BSE, here calculated using only 7 occupied and 4 unoccupied bands. Clearly, the main peak is unchanged whether a $6 \times 6 \times 6$ or a $8 \times 8 \times 8$ grid is used, and it is already very well described using a $4 \times 4 \times 4$ grid. This quite coarse grid yields hence absorption spectra that can be discussed safely. Instead, using the same grid is more delicate when it comes to details of the JDOS, which is not a measurable quantity, but which is sometimes used for discussion, such as in Ref.[54]. Therefore, we show in the present article the convergence of the JDOS in Fig. 11. While, as in the case of the spectrum, the main peaks of the JDOS are well identified by the coarsest **k**-point grid, the slope on the low-energy side ($< \sim 3.7$ eV) of the main peak is changing slowly but noticeably with the grid size, in particular at the onset. This finding, which is closely related to the convergence difficulties pointed out in[70], is independent of the number of bands used, as a comparison of middle and lower panels shows. This delicate behavior of the onset is true only in the BSE JDOS: the analogous changes in the GW-IPA JDOS can hardly be seen. Such a convergence problem in the BSE may be explained by a situation where states λ have coefficients $A_\lambda^{vc\mathbf{k}}$ that are a very narrow distribution with **k**, narrower than the difference between **k**-points of the grid. When one uses a discrete **k**-point grid, $W(\mathbf{q})$ is supposed to be constant with **q** over each grid interval or, as it is routinely done for the point $\mathbf{q} = 0$, one replaces $W(\mathbf{q})$ by the average, i.e., an integral over the interval. This leads to an overestimation of the contribution of the long-range part of the screened Coulomb interaction[70]. The error is not noticeable in simple semiconductors, but can play a role in materials such as the present one, where the electron-hole interaction is very strong. Narrow distribution of coefficients occur in the electron-hole continuum, whereas bound excitons have a broader **k**-distribution (see, e.g., Fig. 4). When the distribution is broader than the intervals of the **k**-grid, the piecewise treatment of $W(\mathbf{q})$ is justified. Since the intensity of the bright excitonic states is much larger than that of unbound states, this explains why the spectrum converges quickly. Moreover, contrary to the spectrum, in the JDOS the weight of discrete states should tend to zero with increasing number of **k**-points. One can therefore safely discuss the absorption spectrum with a $4 \times 4 \times 4$-grid, but not the entire JDOS, especially in the region of the onset between 2.5 and ~ 3.7 eV. Indeed, the presence of a number of bound excitons over a large spectral range, whose energy is stable with the **k**-point sampling, is confirmed even by the larger grids, which explains the stability of the spectrum and, despite the convergence issue, confirms the conclu-

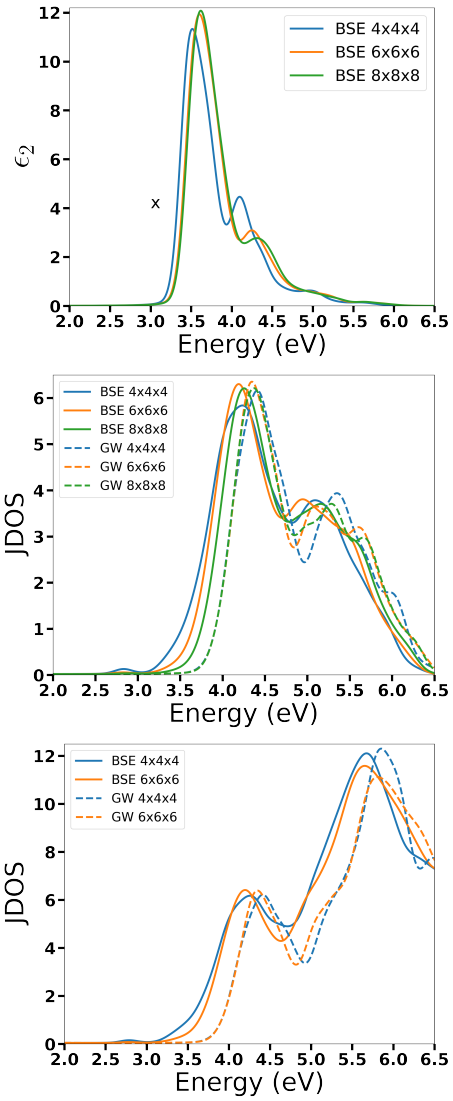

FIG. 11: Convergence with respect to the Brillouin zone sampling of spectral features of V_2O_5 in the ideal crystal structure. Upper panel: BSE absorption spectra along x polarisation direction. Middle and lower panel: JDOS of BSE and GW-IPA for different grids. Middle panel, 7 occupied bands and 4 unoccupied bands. Lower panel: 13 occupied and 10 unoccupied bands.

sions of Ref.[54] concerning the difficulty to determine the onset of the continuum.

2. Scissor-correction approximation

The spectra in Fig. 12 are calculated within the GW-IPA, using different ingredients, for the ideal V_2O_5 (dashed lines) and the structure with the largest distortion for the B^6_{2g} mode (solid lines). In the full calculation (blue curves) the spectra are obtained taking into account the GW corrections (see Eq. (4)) for all the bands and $\mathbf{k}$ points included in the response function. Alternatively, the GW corrections have been approximated in the spectra (green curves) by a rigid scissor correction for the conduction states, equal to the GW band gap opening at the Γ point. We find that the effect of the scissor correction approximation with respect to the full calculation is small. In both cases we find QP corrections with a spread of 0.3-0.4 eV over the different states, but without a clear tendency, such that a large part of the effect averages out in the spectrum. Since the main peaks in the absorption spectrum are less sharp in the distorted than in the ideal structure, this averaging out of the difference with respect to a simple scissor correction is even more efficient. Most importantly, however, the error due to the scissor is in all cases much smaller than the difference between the spectra for the distorted and ideal structures.

In Fig. 12 we also verify, for the GW-IPA spectra of the distorted structure, the use of the screened Coulomb interaction $W_{\rm ideal}$ of the ideal structure instead of $W_{\rm dist}$ of the distorted structure. The comparison is excellent for both the spectra with the full GW corrections (compare blue and orange solid lines) and the spectra obtained with the corresponding scissor corrections (compare green and purple solid lines).

[1] R. M. Martin, L. Reining, and D. M. Ceperley, *Interacting Electrons: Theory and Computational Approaches* (Cambridge University Press, 2016).
[2] D. Pines, *Elementary Excitations In Solids* (Benjamin, New York, 1963).
[3] R. S. Knox, *Theory of Excitons* (Academic Press, 1963).
[4] S. A. Maier, M. L. Brongersma, P. G. Kik, S. Meltzer, A. A. G. Requicha, and H. A. Atwater, Advanced Materials **13**, 1501 (2001).
[5] G. Grosso, J. Graves, A. T. Hammack, A. A. High, L. V. Butov, M. Hanson, and A. C. Gossard, Nature Photonics **3**, 577 (2009).
[6] X.-G. Zhao, Z. Wang, O. I. Malyi, and A. Zunger, Materials Today **49**, 107 (2021).
[7] Z. Wang, O. I. Malyi, X. Zhao, and A. Zunger, Phys. Rev. B **103**, 165110 (2021).
[8] Z. Wang, X.-G. Zhao, R. Koch, S. J. L. Billinge, and A. Zunger, Phys. Rev. B **102**, 235121 (2020).
[9] J. Varignon, M. Bibes, and A. Zunger, Phys. Rev. B **100**, 035119 (2019).
[10] Y. Qin, G. Fan, K. Liu, and M. Hu, Sensors and Actuators B: Chemical **190**, 141 (2014).
[11] A. Dhayal Raj, T. Pazhanivel, P. Suresh Kumar, D. Mangalaraj, D. Nataraj, and N. Ponpandian, Current Applied

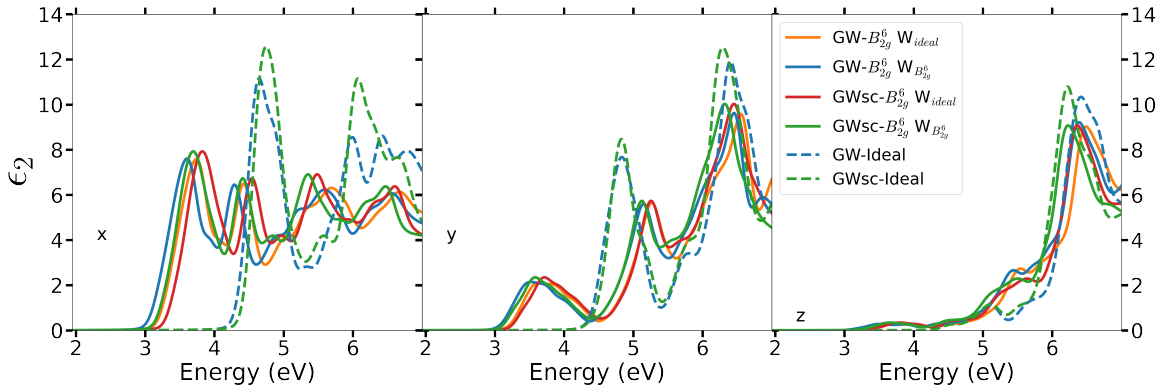

FIG. 12: GW-IPA absorption spectra, in the 3 cartesian polarization directions, (left) x, (middle) y and (right) z, of the crystal structure distorted along the B_{2g}^6 mode with the largest displacements (solid lines) compared to those of ideal crystal structure (dashed lines): full GW-IPA (blue lines) and scissor-corrected (sc) GW-IPA (green lines). For the distorted structure, the full GW spectra (orange lines) and scissor-corrected (sc) GW spectra (purple lines) are also obtained with the screened Coulomb interaction W_{ideal} calculated in the ideal V_2O_5.

Physics **10**, 531 (2010).

[12] S. A. Razek, M. R. Popeil, L. Wangoh, J. Rana, N. Suwandaratne, J. L. Andrews, D. F. Watson, S. Banerjee, and L. F. J. Piper, Electronic Structure **2**, 023001 (2020).

[13] O. Monfort and P. Petrisková, Processes **9**, 214 (2021).

[14] M. Liu, B. Su, Y. Tang, X. Jiang, and A. Yu, Advanced Energy Materials **7**, 1 (2017).

[15] X. Liu, J. Zeng, H. Yang, K. Zhou, and D. Pan, RSC Adv. **8**, 4014 (2018).

[16] Y. Wang, K. Takahashi, K. Lee, and G. Cao, Advanced Functional Materials **16**, 1133 (2006).

[17] B. M. Weckhuysen and D. E. Keller, Catalysis Today **78**, 25 (2003).

[18] N. A. Chernova, M. Roppolo, A. C. Dillon, and M. S. Whittingham, J. Mater. Chem. **19**, 2526 (2009).

[19] Y.-R. Lu, T.-Z. Wu, H.-W. Chang, J.-L. Chen, C.-L. Chen, D.-H. Wei, J.-M. Chen, W.-C. Chou, and C.-L. Dong, Phys. Chem. Chem. Phys. **19**, 14224 (2017).

[20] Y. Fujita, K. Miyazaki, and C. Tatsuyama, Japanese Journal of Applied Physics **24**, 1082 (1985).

[21] R. Enjalbert and J. Galy, Acta Crystallographica Section C **42**, 1467 (1986).

[22] W. Lambrecht, B. Djafari-Rouhani, and J. Vennik, Journal of Physics C: Solid State Physics **14**, 4785 (1981).

[23] C. Bhandari, W. R. L. Lambrecht, and M. Van Schilfgaarde, Physical Review B **91**, 125116 (2015).

[24] M. B. Smirnov, E. M. Roginskii, K. S. Smirnov, R. Baddour-Hadjean, and J.-P. Pereira-Ramos, Inorganic Chemistry **57**, 9190 (2018).

[25] V. Eyert and K.-H. Höck, Physical Review B **57**, 12727 (1998).

[26] A. Jarry, M. Walker, S. Theodoru, L. J. Brillson, and G. W. Rubloff, Chemistry of Materials **32**, 7226 (2020).

[27] S. Suthirakun, S. Jungthawan, and S. Limpijumnong, The Journal of Physical Chemistry C **122**, 5896 (2018).

[28] A. Mukherjee, H. A. Ardakani, T. Yi, J. Cabana, R. Shahbazian-Yassar, and R. F. Klie, Applied Physics Letters **110**, 213903 (2017).

[29] W. Olszewski, I. Isturiz, C. Marini, M. Avila, M. Okubo, H. Li, H. Zhou, T. Mizokawa, N. L. Saini, and L. Simonelli, Physical Chemistry Chemical Physics **20**, 15288 (2018).

[30] G. A. Horrocks, E. J. Braham, Y. Liang, L. R. De Jesus, J. Jude, J. M. Velázquez, D. Prendergast, and S. Banerjee, The Journal of Physical Chemistry C **120**, 23922 (2016).

[31] C. Delmas, H. Cognac-Auradou, J. Cocciantelli, M. Ménétrier, and J. Doumerc, Solid State Ionics **69**, 257 (1994).

[32] V. A. Ioffe and I. B. Patrina, physica status solidi (b) **40**, 389 (1970).

[33] D. O. Scanlon, A. Walsh, B. J. Morgan, and G. W. Watson, Journal of Physical Chemistry C **112**, 9903 (2008).

[34] D. Jesus, R. Luis, G. A. Horrocks, Y. Liang, A. Parija, C. Jaye, L. Wangoh, J. Wang, D. A. Fischer, L. F. J. Piper, D. Prendergast, and S. Banerjee, Nature Communications **7**, 12022 (2016).

[35] P. Watthaisong, S. Jungthawan, P. Hirunsit, and S. Suthirakun, RSC Adv. **9**, 19483 (2019).

[36] L. Ngamwongwan, I. Fongkaew, S. Jungthawan, P. Hirunsit, S. Limpijumnong, and S. Suthirakun, Phys. Chem. Chem. Phys. **23**, 11374 (2021).

[37] G. Onida, L. Reining, and A. Rubio, Rev. Mod. Phys. **74**, 601 (2002).

[38] E. Runge and E. K. U. Gross, Phys. Rev. Lett. **52**, 997 (1984).

[39] C. Ullrich, *Time-dependent Density-functional Theory: Concepts and Applications*, Oxford graduate texts (Oxford University Press, 2012).

[40] G. Strinati, Rivista del Nuovo Cimento **11**, 1 (1988), and references therein.

[41] S. L. Adler, Phys. Rev. **126**, 413 (1962).

[42] N. Wiser, Phys. Rev. **129**, 62 (1963).

[43] L. Hedin, Phys. Rev. **139**, A796 (1965).

[44] M. S. Hybertsen and S. G. Louie, Phys. Rev. B **34**, 5390 (1986).

[45] R. W. Godby, M. Schlüter, and L. J. Sham, Phys. Rev. B **37**, 10159 (1988).

[46] M. van Schilfgaarde, T. Kotani, and S. Faleev, Phys. Rev. Lett. **96**, 226402 (2006).

[47] S. Albrecht, L. Reining, R. Del Sole, and G. Onida, Phys. Rev. Lett. **80**, 4510 (1998).

[48] L. X. Benedict, E. L. Shirley, and R. B. Bohn, Phys. Rev. Lett. **80**, 4514 (1998).

[49] M. Rohlfing and S. G. Louie, Phys. Rev. B **62**, 4927 (2000).
[50] N. Troullier and J. L. Martins, Physical Review B **43**, 1993 (1991).
[51] E. Papalazarou, M. Gatti, M. Marsi, V. Brouet, F. Iori, L. Reining, E. Annese, I. Vobornik, F. Offi, A. Fondacaro, S. Huotari, P. Lacovig, O. Tjernberg, N. B. Brookes, M. Sacchi, P. Metcalf, and G. Panaccione, Phys. Rev. B **80**, 155115 (2009).
[52] M. Gatti, F. Sottile, and L. Reining, Phys. Rev. B **91**, 195137 (2015).
[53] See Supplementary Material for additional details about the convergence studies and the distorted crystal structures.
[54] V. Gorelov, L. Reining, M. Feneberg, R. Goldhahn, A. Schleife, W. R. L. Lambrecht, and M. Gatti, npj Computational Materials **8**, 94 (2022).
[55] X. Gonze, G.-M. Rignanese, M. Verstraete, J.-M. Beuken, Y. Pouillon, R. Caracas, F. Jollet, M. Torrent, G. Zerah, M. Mikami, *et al.*, Z. Kristallogr **220**, 558 (2005).
[56] `http://dp-code.org/`.
[57] `http://www.bethe-salpeter.org/`.
[58] F. Bassani and G. P. Parravicini, *Electronic States and Optical Transitions in Solids* (Pergamon Press, 1975).
[59] M. Feierabend, G. Berghäuser, A. Knorr, and E. Malic, Nature Communications **8**, 14776 (2017).
[60] K.-D. Park, T. Jiang, G. Clark, X. Xu, and M. B. Raschke, Nature Nanotechnology 2017 13:1 **13**, 59 (2017).
[61] S. Kusaba, K. Watanabe, T. Taniguchi, K. Yanagi, and K. Tanaka, Applied Physics Letters **119**, 093101 (2021).
[62] S. Atzkern, S. V. Borisenko, M. Knupfer, M. S. Golden, J. Fink, A. N. Yaresko, V. N. Antonov, M. Klemm, and S. Horn, Physical Review B **61**, 12792 (2000).
[63] C. Bhandari and W. R. L. Lambrecht, Phys. Rev. B **89**, 045109 (2014).
[64] P. Clauws, J. Broeckx, and J. Vennik, physica status solidi (b) **131**, 459 (1985).
[65] P. Clauws and J. Vennik, physica status solidi (b) **76**, 707 (1976).
[66] We note that the LDA gives similar results for V_2O_5 to the generalised gradient approximation[71] (GGA) (see also e.g. Refs.[72–74]). In particular, for the ideal structure, we obtain a GGA band gap of 1.84 eV.
[67] N. Kenny, C. Kannewurf, and D. Whitmore, Journal of Physics and Chemistry of Solids **27**, 1237 (1966).
[68] V. Garbuio, M. Cascella, L. Reining, R. D. Sole, and O. Pulci, Phys. Rev. Lett. **97**, 137402 (2006).
[69] S. S. Dong, M. Govoni, and G. Galli, Chem. Sci. **12**, 4970 (2021).
[70] F. Fuchs, C. Rödl, A. Schleife, and F. Bechstedt, Phys. Rev. B **78**, 085103 (2008).
[71] J. P. Perdew, K. Burke, and M. Ernzerhof, Phys. Rev. Lett. **77**, 3865 (1996).
[72] L. Wang, T. Maxisch, and G. Ceder, Phys. Rev. B **73**, 195107 (2006).
[73] A. Jovanović, A. S. Dobrota, L. D. Rafailović, S. V. Mentus, I. A. Pašti, B. Johansson, and N. V. Skorodumova, Phys. Chem. Chem. Phys. **20**, 13934 (2018).
[74] T. Das, S. Tosoni, and G. Pacchioni, Computational Materials Science **163**, 230 (2019).